

Radiolabeling and PET-MRI microdosing of the experimental cancer therapeutic, MN-anti-miR10b, demonstrates delivery to metastatic lesions in a murine model of metastatic breast cancer

Mariane Le Fur

Harvard Medical School

Alana Ross

Harvard Medical School

Pamela Pantazopoulos

Harvard Medical School

Nicholas Rotile

Harvard Medical School

Iris Zhou

Harvard Medical School

Peter Caravan

Harvard Medical School

Zdravka Medarova

Harvard Medical School

Byunghee Yoo (✉ byoo@mgh.harvard.edu)

Harvard Medical School <https://orcid.org/0000-0001-9066-6399>

Research

Keywords: microRNA, RNA interference, metastasis, biodistribution, positron emission tomography, MR imaging

Posted Date: May 6th, 2021

DOI: <https://doi.org/10.21203/rs.3.rs-459873/v1>

License:  This work is licensed under a Creative Commons Attribution 4.0 International License.

[Read Full License](#)

Version of Record: A version of this preprint was published at Cancer Nanotechnology on July 8th, 2021.
See the published version at <https://doi.org/10.1186/s12645-021-00089-5>.

Abstract

Background

In our earlier work, we identified microRNA-10b (miR10b) as a master regulator of the viability of metastatic tumor cells. This knowledge allowed us to design a miR10b-targeted therapeutic consisting of anti-miR10b and ultrasmall iron oxide magnetic nanoparticles (MN), termed MN-anti-miR10b. In mouse models of breast cancer, we demonstrated that MN-anti-miR10b caused durable regressions of established metastases with no evidence of systemic toxicity. As a first step towards translating MN-anti-miR10b for the treatment of metastatic breast cancer, we needed to determine if MN-anti-miR10b, which is so effective in mice, will also accumulate in human metastases.

Results

In this study, we devised a method to efficiently radiolabel MN-anti-miR10b with Cu-64 (^{64}Cu) and evaluated the pharmacokinetics and biodistribution of the radiolabeled product at two different doses: a therapeutic dose, referred to as macrodose, corresponding to ^{64}Cu -MN-anti-miR10b co-injected with non-labeled MN-anti-miR10b, and a tracer level dose of ^{64}Cu -MN-anti-miR10b, referred to as microdose. In addition, we evaluated the uptake of ^{64}Cu -MN-anti-miR10b by metastatic lesions using both *in vivo* and *ex vivo* positron emission tomography-magnetic resonance imaging (PET-MRI). A comparable distribution of the therapeutic was observed after administration of a microdose or macrodose. Uptake of the therapeutic by metastatic lymph nodes, lungs, and bone was also demonstrated by PET-MRI with a significantly higher PET signal than in the same organs devoid of metastatic lesions.

Conclusion

Our results demonstrate that PET-MRI following a microdose injection of the agent will accurately reflect the innate biodistribution of the therapeutic. The tools developed in the present study lay the groundwork for the clinical testing of MN-anti-miR10b and other similar therapeutics in patients with cancer.

Background

Conventional therapies targeted towards the primary tumor cell oftentimes do not affect the metastatic cell and, in fact, may promote metastasis. This explains the poor outcomes in patients diagnosed with metastatic disease despite the good prognosis of patients with localized cancer of the same organ of origin¹. For these reasons, our research has focused on developing therapies specific to unique properties of metastatic tumor cells. These cells have the ability to break out of the primary tumor mass, travel through the circulation, and colonize a new vital organ in the process of metastasis. Importantly, these cells are genetically and phenotypically distinct from the majority of the cells in the tumor mass,

spawning metastatic lesions that have diverged in their gene expression profile from their respective primary tumors.

In our earlier work, we showed that the metastamir microRNA-10b (miR10b) powerfully promotes the viability of metastatic tumor cells. We confirmed the earlier reports that miR10b promotes the invasion and migration capability of tumor cells^{2,3}. We also demonstrated that miR10b facilitates the survival of metastatic tumor cells^{4,5,6}. Based on this knowledge, we developed a therapeutic strategy against metastatic cancer centered around the inhibition of miR10b in tumors and metastases. The inhibition of miR10b was achieved using antagonists conjugated to ultrasmall iron oxide magnetic nanoparticles (MN), which served as carriers for the antagonists. We termed this novel therapeutic MN-anti-miR10b. We demonstrated that MN-anti-miR10b could completely prevent the formation of *de novo* metastases⁴ and, when combined with a low-dose cytostatic, caused complete and persistent regression of local lymph node and distant metastases in breast cancer models with no evidence of systemic toxicity^{5,6}. Detailed molecular studies showed that the mechanism of action of MN-anti-miR10b is entirely novel and relies on a process which we have termed “metastamir addiction”⁵. Metastamir addiction refers to a property of metastatic tumor cells, according to which they upregulate the expression of specific microRNAs as an adaptive advantage. This advantage promotes the capacity of tumor cells to survive, invade surrounding tissue, and migrate in response to physiological stress caused by insufficient vascular supply, low pH, poor cell-cell contacts, and inadequate extracellular matrix (ECM) support.

From our earlier studies in animal models, we learned that the delivery of MN-anti-miR10b and other MN-based agents to tumors and metastases relies on a combination of hemodynamic, physicochemical, and metabolic factors. The MN nanoparticles are long-circulating^{7,8}. They distribute to the interstitium of tumors and metastases via the enhanced permeability and retention (EPR) effect, followed by cell uptake of the positively charged nanoparticles through macropinocytosis^{9,10,11}.

As a first step towards translating MN-anti-miR10b for the treatment of metastatic breast cancer, we needed to determine if MN-anti-miR10b, which is so effective in mice, will also accumulate in human metastases. Towards that goal, we developed a method to radiolabel MN-anti-miR10b with Cu-64 through a NODAGA chelator. The choice of Cu-64 for radiolabeling was motivated by the fact that the radionuclide has a low b⁺ energy ($E_{b+,max} = 656$ keV), which is comparable to that of ¹⁸F ($E_{b+,max} = 633$ keV) and would ensure a high sensitivity of detection¹². Also, Cu-64 has a 12.7-hr half-life, allowing for adequate assessment of the slow pharmacokinetics of macromolecules or blood-pool agents^{12,13}. The NODAGA chelator was also found to be optimal because it forms a stable complex with Cu-64 and permits the accurate determination of the biodistribution of the radiolabeled entity^{14,15,16}.

In the current study, a microdose of ⁶⁴Cu-MN-anti-miR10b was injected into murine models of metastatic breast cancer. Its uptake by the metastatic lesions was determined using simultaneous positron emission tomography-magnetic resonance imaging (PET-MRI). PET-MRI clearly demonstrated uptake of ⁶⁴Cu-MN-anti-miR10b by the metastatic lesions, measurable at a microdose. *Ex vivo* PET-MRI confirmed that the

activity was associated with the metastatic lesions, as identified at necropsy. Uptake by metastatic organs was also demonstrated through ex vivo quantification by gamma counting and shown to be significantly higher than in the same organs devoid of metastatic lesions. Finally, we demonstrated that a microdose of ^{64}Cu -MN-anti-miR10b showed the same biodistribution as a standard therapeutic dose. These preclinical studies set the stage for a clinical investigation of ^{64}Cu -MN-anti-miR10b delivery to human metastases, which represents a critical step towards translating this and other similar nanotherapeutics.

Materials And Methods

General methods. All reactants and reagents were of commercial grade and were used without further purification. All solutions were prepared from MilliQ water. Metal-free buffer solutions used for radiolabeling were prepared using Chelex 100 Resin (100-200 mesh, BioRad). All animal experiments were performed in compliance with institutional guidelines and approved by the Institutional Animal Care and Use Committee at Massachusetts General Hospital (Boston, MA).

Synthesis of NODAGA-MN-anti-miR10b.

The steps for the synthesis of $^{\text{nat}}/\text{Cu}$ -MN-anti-miR10b are outlined in **Scheme 1**. Amine-derivatized iron oxide nanoparticles (MN) were prepared from dextran-coated iron oxide nanoparticles through modification with epichlorohydrin and ammonium hydroxide as described previously¹⁷. The nanoparticles were conjugated with NODAGA-NHS (Chematech, France) by reacting 1 ml of MN (87 μM , 10 mg Fe/ml, 54 NH₂/MN) with 2.54 mg of NODAGA-NHS ester (3.47 mmol, 40 eq. to MN) in 100 μl PBS buffer (100 mM, pH 7.4). The reaction was carried out overnight at 4°C, then the resulting NODAGA-conjugated nanoparticles (NODAGA-MN) were purified with a size exclusion column (PD-10, GE Healthcare) using nuclease free PBS buffer as an eluent. NODAGA-MN was treated with excess amounts of SPDP (250 eq.) for 4 hrs at 4°C to form NODAGA-MN-SPDP, which was again purified with a size exclusion column using nuclease free PBS buffer as an eluent. The LNA antagonir, anti-miR10b is synthesized and provided by Biospring (Frankfurt, Germany) following a GLP protocol. The anti-miR10b LNA antagonir was modified with the 5'-Thiol-Modifier C6 disulfide (5'-ThioMC6), which was utilized for conjugation to MN. The disulfide on the oligonucleotide was activated by 3% Tris (2-carboxyethyl) phosphine hydrochloride (TCEP, Thermoscientific Co.), followed by purification with ammonium acetate/ethanol precipitation treatment prior to conjugation to MN. After TCEP activation and purification, the oligo was dissolved in nuclease free water and incubated with NODAGA-MN-SPDP overnight. The final product, NODAGA-MN-anti-miR10b, was freshly prepared prior to animal studies.

Preparation of non-radioactive $^{\text{nat}}\text{Cu}$ -MN-anti-miR10b

Nonradioactive $^{\text{nat}}\text{Cu}$ -MN-anti-miR10b was prepared to evaluate the inhibitory effect of miR-10b in 4T1 cells. 0.6 mg Fe of NODAGA-MN-anti-miR10b were dispersed in acetate buffer (500 μL , pH 6.8, 0.1 M) followed by the addition of CuCl₂ (0.7 mg, 50 equiv. Cu²⁺ to NODAGA). The reaction mixture was stirred at

60°C for 20 min and EDTA (100 µL, 100 mM, pH 7.4) was added to the mixture to remove any unlabeled free Cu²⁺ ions followed by purification with size exclusion column (PD-10, GE Healthcare) using nuclease free PBS buffer as an eluent. Fractions containing the desired product were combined and the concentration of ^{nat}Cu-MN-anti-miR10b was determined by ICP-MS.

Preparation of radiolabeled MN-anti-miR10b (⁶⁴Cu-MN-anti-miR10b)

Radiolabeling was performed following commonly used procedures ¹⁸. Briefly, 200 µg (as Fe) of NODAGA-MN-anti-miR10b in PBS was added to a solution of ⁶⁴CuCl₂ (4 mCi, 148 MBq, the University of Wisconsin at Madison, WI) in sodium acetate buffer (0.1 M, pH 6.8, 500 µL). The reaction mixture was heated at 60°C for 20 min and then purified with a size exclusion column (PD-10 column) using nuclease free PBS buffer as an eluent and each 500 µL of eluent was collected as a fraction. The radiochemical purity of each fraction was controlled by iTLC (Agilent, iTLC-SG, Santa Clara, CA) with an EDTA solution as an eluent (50 mM, pH 5) using a radio-TLC imaging scanner (AR-2000, Eckert & Ziegler, Berlin, Germany). Fractions with a radiochemical purity > 99% were combined and used for in vivo animal studies. Radiochemical identity of the final solution of ⁶⁴Cu-MN-anti-miR10b was confirmed by analytical HPLC (Agilent 1100 HPLC system, Santa Clara, CA) with a size exclusion column (TSK gel QC-PAK-300, isocratic, 100% sodium phosphate 0.1 M pH 7.4, 20 min) and a Carroll/Ramsey radioactivity detector with a silicon PIN photodiode and with UV detection at 254 nm.

Characterization of MN-anti-miR10b and ^{nat}Cu-MN-anti-miR10b

ICP-MS analysis (Agilent 8800-QQQ system, Santa Clara, CA) was carried out to determine the concentrations of copper and iron. All samples were prepared by weight. Calibration standards were prepared by diluting certified copper and iron standards (1000 mg/L). Calibration curve was obtained from 5 standard solutions in the range from 0.1 to 400 ppb. Lutetium (1 ppm) was used as an external standard to ensure the proper introduction of the sample. The hydrodynamic diameter and Zeta-potential were measured by a dynamic light scattering spectrometer (Zetasizer Nano, Malvern, UK) and the size of the iron oxide core was determined by transmission electron microscopy (JEM 2100 TEM, Jeol, Tokyo, Japan). To quantify the number of NODAGA per MN, the number of amines per MN was subtracted from the number of amines per MN after conjugation with NODAGA. The number of amines per MN was quantified by pyridine-2-thione (343nm, 8080 M⁻¹cm⁻¹) released from SPDP that was conjugated to the amine groups at a one-to-one ratio (ThermoFisher, Waltham, MA). Finally, the number of oligonucleotides per MN was determined by spectrophotometry with multiple standards of different concentrations. Briefly, MN-anti-miR10b and ^{nat}Cu-MN-anti-miR10b were purified using a magnetic column (MACS column, Miltenyi, Cambridge, MA) to remove unbound anti-miR10b oligo. The purified nanoparticles were assayed to determine iron concentration (410 nm) and the concentration of oligo (260 nm) by spectrophotometry (Spectramax M2 microplate reader, Molecular Devices, Sunnyvale, CA).

Cellular uptake

The cellular uptake of ^{nat}Cu-MN-anti-miR10b was compared with that of MN-anti-miR10b and parent MN. 4T1-luc cells were seeded in a 12-well plate and incubated with ^{nat}Cu-MN-anti-miR10b, MN-anti-miR10b, and MN for 24 hrs at 37 °C. After washing with DPBS, the cells were lysed (Cell lysis buffer, Sigma-Aldrich, St. Louis, MO) and analyzed by ICP-MS to determine the concentration of iron. The protein concentration was determined by BCA assay (Sigma-Aldrich, St. Louis, MO). The cellular uptake of nanoparticles was normalized by total protein.

Real-time quantitative reverse transcription-PCR

To assess target engagement by ^{nat}Cu-MN-anti-miR10b as compared to the unlabeled MN-anti-miR10b, 4T1-luc cells were incubated with ^{nat}Cu-MN-anti-miR10b, MN-anti-miR10b, and MN for 48 hrs at 37 °C. From the cell lysates, the microRNA-enriched fraction was harvested using a miRNeasy mini kit following the manufacturer's protocol (Qiagen Inc., Hilden, Germany). Relative expression of miR-10b was determined by real-time quantitative reverse transcription-PCR (qRT-PCR; Taqman protocol) and normalized to the internal housekeeping gene, SNORD44. Taqman analysis was carried out using an ABI Prism 7700 sequence detection system (Applied Biosystems, Foster City, CA). The primers (Hs-miR-10b-3 miScript Primer, Hs-SNORD44-11 miScript Primer) and assay kit (miScript PCR Starter Kit, Qiagen, Hilden, Germany).

Animal model and administration of ⁶⁴Cu-MN-anti-miR10b.

Eight-week-old female Balb/c mice (The Jackson Laboratory; Bar Harbor, ME) were implanted orthotopically under the top right third mammary fat pad with the 4T1-Red-Fluc cell line (0.5×10^6 cells). The cells express luciferase and can be detected by non-invasive bioluminescence imaging (BLI) for corresponding analysis of tumor burden. All animals were scanned by BLI to keep track of metastasis formation twice a week. Two weeks after cell inoculation, mice were injected intravenously with ⁶⁴Cu-MN-anti-miR10b. For the microdosing studies, ⁶⁴Cu-MN-anti-miR10b prepared as described above, was injected at a dose of 20 mg as Fe, 118-190 mCi per mouse, n = 6. For the carrier-added macrodosing studies, ⁶⁴Cu-MN-anti-miR10b was mixed with NODAGA-MN-anti-miR10b and injected at a dose of 300 µg as Fe, 127-135 µCi per mouse, n = 7. An aliquot of the injected dose was analyzed for %ID/g calculations.

After PET-MR imaging, mice were sacrificed at 24 hr post injection (n = 3 in microdose group and n = 4 in macrodose group) and 48 hr post injection (n = 3 in each group) for ex vivo biodistribution analysis.

Bioluminescence optical imaging (BLI)

BLI was used to identify metastases. Imaging was performed using the IVIS Spectrum imaging system (Perkin Elmer, Hopkinton, MA). Anesthetized mice were injected intraperitoneally with D-luciferin potassium salt in DPBS (200 mL of 15 mg/mL; Perkin Elmer, Hopkinton, MA) 12 minutes before image acquisition. Identical imaging acquisition settings (time, ~ 0.5–60 seconds; F-stop, 2; binning, medium) and the same ROI were used to obtain total radiance (photons/sec/cm²/sr) over the whole body. BLI was

performed for about 6 to 15 minutes to obtain the maximum radiance. All images were processed using the Living Image Software (ver 4.5, IVIS Spectrum, Perkin Elmer, Hopkinton, MA). The total radiance from the bioluminescence readings was used for signal quantification.

PET-MR imaging

Mice were imaged in a 4.7 Tesla MRI scanner equipped with a PET insert (Bruker, Billerica MA). Mice were anesthetized with 1-2% isoflurane in medical air. Mice were kept warm using an air heater system and body temperature and respiration rate monitored by a physiological monitoring system (SA Instruments Inc., Stony Brook NY) throughout the imaging session. For the microdosing studies, dynamic PET acquisition was performed continuously for 1 hr after injection of ^{64}Cu -MN-anti-miR10b. Mice were then returned to their cages and imaged again at 2 hr, 4 hr, 24 hr and 48 hr post-injection for a period of 30 mins, 30 mins, 60 mins, and 60 mins, respectively. For the macrodosing studies, mice were scanned at 24 hr after injection of ^{64}Cu -MN-anti-miR10b for 60 mins. For ex-vivo imaging, organs were positioned onto a plastic holder and scanned for 15 minutes.

Anatomic MR images were obtained simultaneously with PET acquisition, including T1-weighted 3D FLASH (Fast Low Angle Shot) sequences with the following parameters: echo time (TE) = 3 ms, repetition time (TR) = 20 ms, imaging resolution = $0.25 \times 0.25 \times 0.5 \text{ mm}^3/\text{voxel}$, and flip angle = 12 degrees.

PET-MR imaging data were analyzed to estimate the biodistribution and clearance of ^{64}Cu -MN-anti-miR10b. Regions of interest (ROIs) were drawn on the MR images over major organs, including heart, liver and kidneys using AMIDE software package ¹⁹, and used for quantifying radioactivity for each PET frame. The uptake of ^{64}Cu -MN-anti-miR10b in metastases and corresponding tissues without metastases was quantified using ROIs over metastatic bone and lymph node identified by BLI and their non-metastatic contralateral counterparts. Results were expressed as percentage of injected dose per cubic centimeter of tissue (%ID/cc).

Ex vivo biodistribution

Animals were sacrificed at 24 hr and 48 hr post injection. The following organs and tissues were collected: lymph nodes, blood, urine, kidneys, liver, spleen, pancreas, heart, lungs, brain, femur, bladder and muscle. After resection and ex vivo scanning, organs were weighed and the counts in each organ were measured using a gamma counter (Wizard, Perkin Elmer) with correction for decay.

Statistical Analysis

Data were expressed as mean \pm s.d. Statistical comparisons were made using a two-tailed t-test using GraphPad Prism software. A P value of less than 0.05 was considered statistically significant.

Results

Synthesis and characterization of ^{nat}/⁶⁴Cu-MN-anti-miR10b.

The synthesis of ⁶⁴Cu-MN-anti-miR10b started with the modification of MN, a 20-nm aminated dextran-coated iron oxide nanoparticle whose synthesis was previously reported ¹⁷. The nanoparticles have been optimized to enhance the extravasation of the agent into the interstitium of tumors and metastatic lesions ²⁰. MN nanoparticles were functionalized with NODAGA, a chelating ligand, by a coupling reaction between the amino groups and the activated ester moiety of NODAGA (**Scheme 1**). We chose the NODAGA chelator because of its ability to rapidly form highly stable ⁶⁴Cu complexes, essential for preventing in vivo dissociation of the radiometal and its subsequent retention in the body. The number of NODAGA chelators per nanoparticle was quantified as 13 ± 2 . The ratio of Cu/nanoparticle was determined as 14 ± 1 by ICP-MS after complex formation using ^{nat}CuCl₂. Prior to in vivo studies, the nanoparticles were treated with SPDP and functionalized with anti-miR-10b antagonists via a disulfide linkage. The number of antagonists per nanoparticle was characterized as 7.4 ± 0.2 following previously described procedures ^{5,17}.

Evaluating the *in vivo* biodistribution of ⁶⁴Cu-MN-anti-miR10b requires the development of efficient labeling and purification methods. The radiolabeling of MN-anti-miR10b was achieved in acetate buffer at pH 6.8, 60°C for 20 minutes. These conditions are favorable for the labeling of NODAGA chelators while maintaining the integrity of the nanocarrier. After purification on a PD-10 column, ⁶⁴Cu-MN-anti-miR10b was obtained with a radiochemical purity >99% (**Figure 1a**) with a specific activity of 7.1 mCi/mg of iron. Radiochemical identity was confirmed by size-exclusion chromatography (**Figure 1b**). In addition, ^{nat}Cu-MN-anti-miR10b was synthesized to evaluate the effect of the presence of Cu-NODAGA chelates on the nanoparticle size and target engagement. The size of the iron oxide core was measured as 4.71 ± 0.24 nm for ^{nat}Cu-MN-anti-miR10b and 4.69 ± 0.23 nm for MN. The surface modifications did not cause any significant changes in the size and crystal structure of the iron oxide core as shown by transmission electron microscopy (TEM, **Figure 1c**). The hydrodynamic diameter of ^{nat}Cu-MN-anti-miR10b was determined as 27.1 ± 0.9 nm, which is 5.1 nm larger than parent MN. The introduction of NODAGA and the anti-miR10b antagonist resulted in a 23 % increase of hydrodynamic diameter (**Figure 1d**).

The cellular uptake, expressed as elemental iron per cell was 9.33 ± 2.42 pg Fe per cell for MN-anti-miR10b and 11.34 ± 3.62 pg Fe per cell for ^{nat}Cu-MN-anti-miR10b, which was not significantly different (**Figure 1e**). Finally, the RNA-enriched cell extracts were analyzed to compare the inhibition of miR10b by qRT-PCR. Compared with the expression level of miR10b after treatment with parent MN devoid of antagonist, miR10b expression was completely inhibited following treatment with MN-anti-miR10b or ^{nat}Cu-MN-anti-miR10b (**Figure 1f**).

Biodistribution of ⁶⁴Cu-MN-anti-miR10b

Next, we evaluated the biodistribution of ⁶⁴Cu-MN-anti-miR10b by PET-MRI and ex vivo gamma counting in a total of 13 mice bearing luciferase-expressing metastatic breast adenocarcinomas (4T1-luc2). 4T1-

luc2 cells express luciferase and can be detected by non-invasive bioluminescence imaging (BLI). Two different concentrations of ^{64}Cu -MN-anti-miR10b were investigated: 1) a tracer level dose of ^{64}Cu -MN-anti-miR10b, referred to as microdose (1 mg Fe/kg, n = 6), and 2) a therapeutic dose, referred to as macrodose, corresponding to ^{64}Cu -MN-anti-miR10b co-injected with MN-anti-miR10b (15 mg Fe/kg, n = 7). Mice were scanned by PET-MRI at different time points. After *in vivo* imaging, the mice were sacrificed at 24 h p.i. (n = 3 in the microdose group and n = 4 in the macrodose group) and 48 h p.i. (n = 3 in each group) for *ex vivo* biodistribution evaluation (**Figure 2**). Time-activity curves for liver, kidney and heart obtained from the PET images (**Figure S1**) indicate that most of the injected dose is rapidly taken up by the liver. This is in line with previously reported studies^{21, 22, 23}.

This is also supported by the *ex vivo* biodistribution analysis indicating that most of the injected dose was present in the liver and the spleen with %ID/g values in the liver of 61.2 ± 6.5 (24h, microdose), 53.4 ± 7.1 (24h, macrodose), 54.3 ± 5.5 (48h, microdose) and 32.1 ± 13.0 (48h, macrodose) (**Figure 2**). %ID/g values lower than 4 were measured in all other harvested organs and tissues. A comparable biodistribution was observed between the microdose and the macrodose at 24h and 48h post injection (**Figures 2a, 2b and S2**, note the presence of metastatic lesions in lymph node, brain, lung and bone). This is also reflected by the strong correlation with slope near unity that is observed between the %ID/g obtained after administration of a microdose and the %ID/g obtained after administration of a macrodose at 24 h and 48 h p.i. in non-metastatic organs, with a Pearson coefficient of 0.91 (p < 0.0001, slope = 1.38) and 0.78 (p = 0.004, slope = 1.05), respectively (**Figure 2c, 2d**).

PET-MRI of ^{64}Cu -MN-anti-miR10b accumulation in tumors and metastases

Two weeks after orthotopic tumor cell implantation, once metastases were confirmed by BLI, the mice were injected intravenously with ^{64}Cu -MN-anti-miR10b. The metastatic organs were identified by *in-vivo* and *ex-vivo* BLI. The uptake of ^{64}Cu -MN-anti-miR10b by metastases was evaluated by PET-MRI following injection of a no-carrier added microdose (20 mg as Fe, 118-190 mCi per mouse, n = 6) or a carrier-added macrodose, as specified above (300 µg as Fe, 127-135 µCi per mouse, n = 7). After *in vivo* PET-MR imaging, the mice were sacrificed at 24 h and 48 h p.i. for *ex vivo* PET-MR imaging.

Consistent with the results from the biodistribution studies, the liver and spleen demonstrated a very high PET signal, indicative of hepatic clearance. Bone and lymph node metastatic lesions could be identified by *in vivo* PET-MRI, partly because of their spatial separation from the liver and spleen (**Figure 3a**). Time-activity curves from metastatic and non-metastatic bones after injection of a microdose of ^{64}Cu -MN-anti-miR10b showed higher uptake by metastases (**Figure S3**). At 24-hr after injection of microdose or macrodose of ^{64}Cu -MN-anti-miR10b, the metastatic lymph nodes and bone identified by BLI showed significantly higher %ID/cc than the corresponding organs devoid of metastases (**Figure 3b**).

BLI images of bone metastatic lesions after injection of a microdose of ^{64}Cu -MN-anti-miR10b are shown in **Figure 3c**. The uptake of ^{64}Cu -MN-anti-miR10b by metastatic lesions was further confirmed by *ex vivo*

PET-MRI (**Figure 3c**). The metastatic bone and lymph nodes could be identified by *in vivo* BLI. These metastatic lesions exhibited higher *ex vivo* PET signal than their non-metastatic counterparts.

In agreement with *ex vivo* biodistribution and *in vivo* PET-MRI, *ex vivo* imaging showed that the activity associated with the excised liver and spleen was highest in both the macrodosing and microdosing studies. High activity was also seen in organs colonized by tumor cells, such as the lymph nodes, bone, and lungs (**Figure 3d**).

Taken together, these observations support a methodology for radiolabeling and imaging of MN-anti-miR10b and other similar nanotherapeutics. Our findings point to the feasibility of clinical PET-MRI of therapeutic accumulation in metastatic lesions, as a critical step on the path to translation of related therapeutic agents.

Discussion

We previously identified microRNA-10b as a master regulator of the viability of metastatic tumor cells and designed the therapeutic miR-10b inhibitor, MN-anti-miR10b, for the treatment of metastatic cancer^{3,4,5}. We demonstrated that MN-anti-miR10b caused complete and persistent regression of local lymph node and distant metastases in breast cancer models with no evidence of systemic toxicity^{5,6}.

In this study, we performed key translational experiments that will bring us closer to applying MN-anti-miR10b in patients with advanced metastatic cancer. We developed a radio-labeled derivative of the MN-anti-miR10b therapeutic, ⁶⁴Cu-MN-anti-miR10b. We demonstrated that radiolabeling the therapeutic did not affect its physico-chemical properties, did not impact cellular uptake *in vitro*, and preserved effective engagement of its target, based on the complete inhibition of miR10b in tumor cells. We then showed that microdosing PET-MRI would adequately reflect the biodistribution of a therapeutic dose of the agent and be effective at highlighting metastatic tissues, based on their uptake of ⁶⁴Cu-MN-anti-miR10b.

The tools and methods described here would allow us to demonstrate delivery of the therapeutic to clinical metastases and clarify the biodistribution of the agent in cancer patients. Indeed, one of the major challenges facing the development of similar therapeutics lies in the effective delivery to the target organs. In the case of drug delivery to metastases, complicating factors include the larger size of the lesions, as compared to animal models, the heterogeneity of human disease, and differences in the pharmacokinetics of the drugs, due to interspecies hemodynamic variability. Based on these differences, it is not possible to directly extrapolate proof of successful clinical implementation of therapeutic agents from pre-clinical biodistribution and efficacy data.

For that reason, the capacity to carry out microdosing PET studies in patients under an exploratory investigational new drug application protocol represents an important step on the path to clinical approval. Since the PET technique is sensitive enough to determine the concentration of radiolabeled drug with sensitivity approaching the subpicomolar range, as little as a microgram of the radiolabeled drug is generally sufficient to perform the proposed PET study in humans. This characteristic has

significant advantages in the initial phases of drug development. Because the low mass of the radiolabeled drug does not induce drug effects, approval from the U.S. Food and Drug Administration for initial human studies may be obtained more quickly and with a more limited preclinical safety and toxicology dossier than is required for therapeutic agents.

Nevertheless, it is not obvious that the microdose will show a linear relationship to the biodistribution and pharmacokinetics of a therapeutic dose. Even though for intravenous compounds there is generally a direct proportionality within a two-fold range²⁴, non-linearity of the relationship is possible due to saturation of absorption, distribution, metabolism and excretion (ADME) at the high doses, and saturation of the target at the low doses. The latter reason is particularly common for monoclonal antibodies, which demonstrate a shorter half-life at low doses because of engagement with limited quantities of endogenous target antigen²⁵. However, in the present study, the fact that we see the same behavior between the microdose and therapeutic dose indicates that it is reasonable to move forward with a microdosing study in patients.

The impact of such an exploratory imaging study would be three-fold. First it would establish that MN-anti-miR10b, which is so effective in mice, will also accumulate in human metastases. This greatly de-risks the clinical development of the therapeutic because it shows drug delivery is indeed feasible. Nanotherapeutics have failed because of poor delivery and the fact that human tumors are larger than in mice with different surface-to-volume ratios. Second, the proposed studies will reveal the pharmacokinetic behavior of MN-anti-miR10b which will allow one to establish dosing during therapy. Third, once MN-anti-miR10b reaches clinical trials, one can use the radiolabeled drug to select patients for treatment, based on which patients' metastases accumulate the therapeutic.

The successful synthesis and testing of ⁶⁴Cu-MN-anti-miR10b is also significant because it sets a precedent for the testing of similar nanotherapeutics. With specific relevance to RNA-based therapeutics, the vast majority of these agents rely on a delivery vehicle, which in many cases comprises a lipid nanoparticle (e.g., Alnylam's Onpattro, MedImmune's MEDI1191 and AstraZeneca's AZD8601) or GalNAc (e.g., Alnylam's Givlaari, Novartis' Inclisiran, etc.). In some of these cases, it may be possible to employ a related radiolabeling and imaging protocol on the path to full clinical trials, in order to not only de-risk clinical development by demonstrating successful delivery but also to gain further insight into target engagement as a function of dose, schedule, or drug design.

Conclusions

The value of clinical microdose imaging studies will be in answering one of the most key questions on the path to drug development without the associated cost to do a full clinical trial – the question of delivery to the target organ sites. In this study, we developed a radiolabeled MN-anti-miR10b therapeutic by introducing NODAGA and radioactive ⁶⁴Cu. The biodistribution of ⁶⁴Cu-MN-anti-miR10b was investigated after the injection of a microdose, which showed a comparable biodistribution to the

therapeutic macrodose in all organs. We expect that the described radiolabeling and imaging protocols will advance the clinical development of similar nanotherapeutics by elucidating the pharmacokinetic behavior of the agents, de-risking future clinical trials, and assisting in the selection of patients for treatment, based on which patients' metastases accumulate the therapeutics.

Declarations

Ethics approval and consent to participate

Not applicable

Consent for publication

All authors reviewed and agreed with the publication of this manuscript in this journal

Availability of data and materials

The datasets generated during and/or analyzed during the current study are available from the corresponding authors on reasonable request.

Competing Interests

Zdravka Medarova is Founder and has equity in TransCode Therapeutics, Inc.

Peter Caravan has equity in Reveal Pharmaceuticals. He has equity in and is a consultant to Collagen Medical LLC. Peter Caravan has research support from Pliant Therapeutics, Indalo Therapeutics, Celgene, Takeda, and Janssen. None of these interests are related to this work.

Funding

This work was supported in part by R01CA16346101A1 from the National Cancer Institute to ZM and S10OD010650, S10OD023503, and S10OD025234 from the NIH Office of the Director for instrumentation to PC. This work was performed in part at the Center for Nanoscale Systems (CNS), a member of the National Nanotechnology Coordinated Infrastructure Network (NNCI), which is supported by the National Science Foundation under NSF award no. 1541959. CNS is part of Harvard University.

Authors' Contributions

MLF performed the radiolabeling and the analysis of oligo-nanoparticles and interpreted *ex vivo* and *in vivo* imaging data and was a major contributor in writing the manuscript. AR prepared animal models and harvested organs for *ex vivo* studies. PP cultured cells for tumor models. NR collected PET-MRI images and IZ analyzed *in vivo* imaging data. BY prepared nanoparticles with RNA oligo and metal ligands. PC, ZM and YB directed the studies, confirm the experimental results and finalize the manuscript. All authors read and approved the final manuscript.

Acknowledgements

Not applicable

References

1. Steeg, P. S. Targeting metastasis. *Nat. Rev. Cancer* **16**, 201-218 (2016).
2. Ma, L. *et al.* Therapeutic silencing of miR-10b inhibits metastasis in a mouse mammary tumor model. *Nat. Biotechnol.* **28**, 341-347 (2010).
3. Ma, L., Teruya-Feldstein, J. & Weinberg, R. A. Tumour invasion and metastasis initiated by microRNA-10b in breast cancer. *Nature* **449**, 682-688 (2007).
4. Yigit, M. *et al.* Context-dependent differences in miR-10b breast oncogenesis can be targeted for the prevention and arrest of lymph node metastasis. *Oncogene* **32**, 1530-1538 (2013).
5. Yoo, B. *et al.* Combining miR10b-targeted nanotherapy with low-dose doxorubicin elicits durable regressions of metastatic breast cancer. *Cancer Res.* **75**, 4407-4415 (2015).
6. Yoo, B. *et al.* Therapy targeted to the metastatic niche is effective in a model of stage IV breast cancer. *Sci. Rep.* **7**, 45060 (2017).
7. Arami, H., Khandhar, A., Liggitt, D. & Krishnan, K. M. In vivo delivery, pharmacokinetics, biodistribution and toxicity of iron oxide nanoparticles. *Chem. Soc. Rev.* **44**, 8576-8607 (2015).
8. Sharma, A. *et al.* Physical characterization and in vivo organ distribution of coated iron oxide nanoparticles. *Sci. Rep.* **8**, 4916 (2018).
9. Juliano, R. L. The delivery of therapeutic oligonucleotides. *Nucleic Acids Res.* **44**, 6518-6548 (2016).
10. Medarova, Z., Pham, W., Farrar, C., Petkova, V. & Moore, A. In vivo imaging of siRNA delivery and silencing in tumors. *Nat. Med.* **13**, 372-377 (2007).
11. Moore, A., Medarova, Z., Potthast, A. & Dai, G. In vivo targeting of underglycosylated MUC-1 tumor antigen using a multimodal imaging probe. *Cancer Res.* **64**, 1821-1827 (2004).
12. Williams, H. A., Robinson, S., Julyan, P., Zweit, J. & Hastings, D. A comparison of PET imaging characteristics of various copper radioisotopes. *Eur. J. Nucl. Med. Mol. Imaging* **32**, 1473-1480 (2005).
13. Woo, S-K. *et al.* Evaluation the human projected Cu-64 labeled radiopharmaceutical internal dosimetry using small animal biodistribution data. *J. Nucl. Med.* **59**, 1014-1014 (2018).
14. Desogere, P. *et al.* Collagen-targeted PET probes for pulmonary fibrosis imaging: effect of the radioisotope on biodistribution. *J. Nucl. Med.* **56**, 6-6 (2015).
15. Roosenburg, S. *et al.* PET and SPECT imaging of a radiolabeled minigastrin analogue conjugated with DOTA, NOTA, and NODAGA and labeled with 64Cu, 68Ga, and 111In. *Mol. Pharm.* **11**, 3930-3937 (2014).
16. Pretze, M., van der Meulen, N. P., Wängler, C., Schibli, R. & Wängler, B. Targeted 64Cu-labeled gold nanoparticles for dual imaging with positron emission tomography and optical imaging. *J. Labelled*

*Comp. Radiopharm.***62**, 471-482 (2019).

17. Yoo, B., Ghosh, S.K., Kumar, M., Moore, A., Yigit, M.V. & Medarova, Z. Design of nanodrugs for miRNA targeting in tumor cells. *J. Biomed. Nanotechnol.***10**, 1114-1122 (2014).
18. Désogère, P. *et al.* Optimization of a collagen-targeted PET probe for molecular imaging of pulmonary fibrosis. *J. Nucl. Med.***58**, 1991-1996 (2017).
19. Loening, A. M. & Gambhir, S. S. AMIDE: a free software tool for multimodality medical image analysis. *Mol. Imaging***2**, 131-137 (2003).
20. Yoo, B., Billig, A-M. & Medarova, Z. Guidelines for Rational Cancer Therapeutics. *Front. Oncol.***7**, 310 (2017).
21. Schlachter, E. K. *et al.* Metabolic pathway and distribution of superparamagnetic iron oxide nanoparticles: in vivo study. *Int. J. Nanomedicine***6**, 1793-1800 (2011).
22. Briley-Saebo, K., Björnerud, A., Grant, D., Ahlstrom, H., Berg, T. & Kindberg, G. M. Hepatic cellular distribution and degradation of iron oxide nanoparticles following single intravenous injection in rats: implications for magnetic resonance imaging. *Cell Tissue Res.***316**, 315-323 (2004).
23. Estevanato, L. L. *et al.* Long-term biodistribution and biocompatibility investigation of dextran-coated magnetite nanoparticle using mice as the animal model. *J. Biomed. Nanotechnol.***8**, 301-308 (2012).
24. van Nuland, M., Rosing, H., Huitema, A. D. R. & Beijnen, J. H. Predictive Value of Microdose Pharmacokinetics. *Clin. Pharmacokinet.***58**, 1221-1236 (2019).
25. Burt, T. *et al.* Phase 0/microdosing approaches: time for mainstream application in drug development? *Nat. Rev. Drug Discov.***19**, 801-818 (2020).

Figures

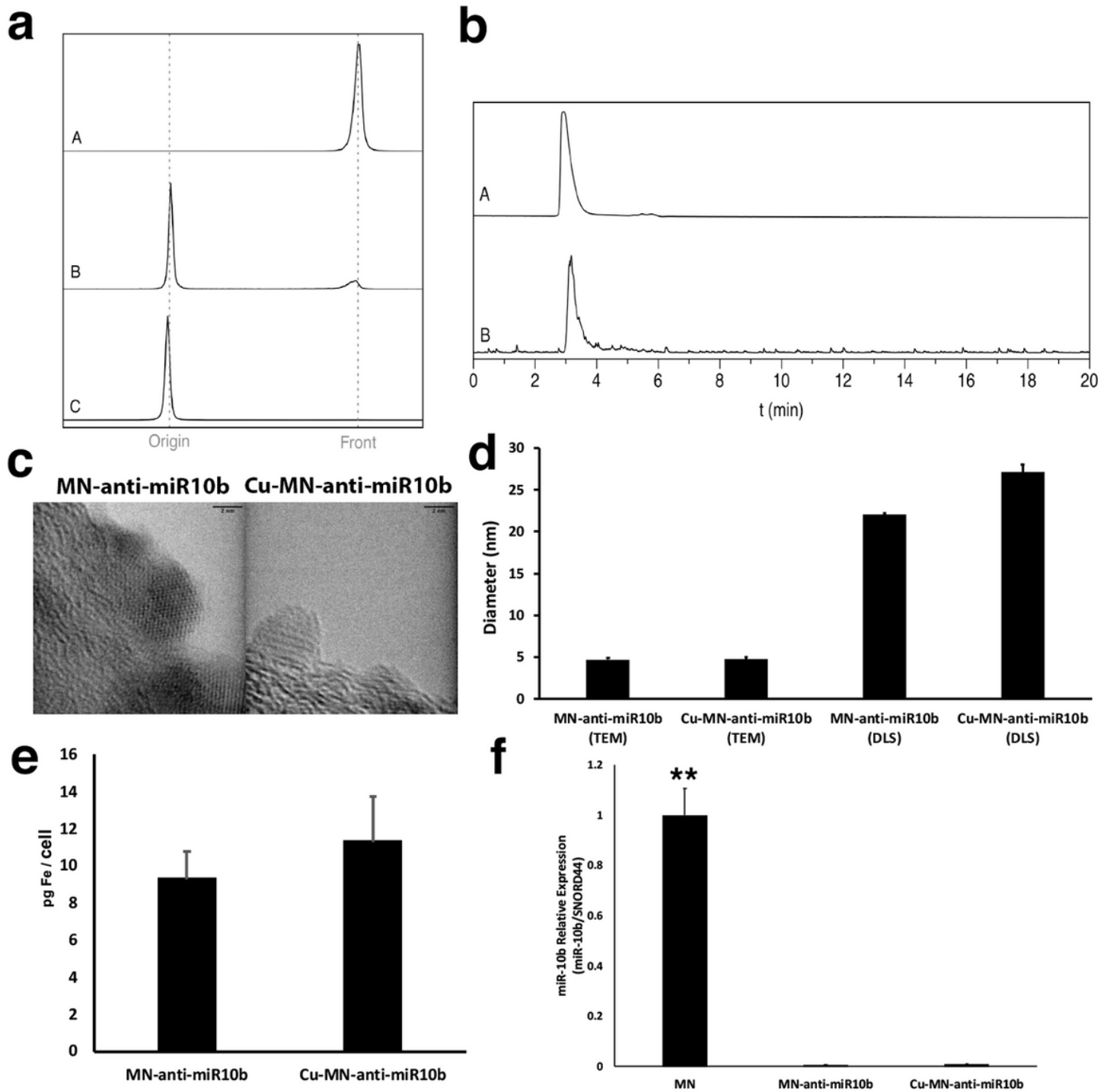


Figure 1

Characterization of nat/64Cu-MN-anti-miR10b. a. Radiochemical purity confirmed by iTLC. (top) unlabeled Cu-64, (middle) separation of 64Cu-MN-anti-miR10b and unlabeled Cu-64, and (bottom) 64Cu-MN-anti-miR10b after PD-10 purification. b. HPLC traces of 64Cu-MN-anti-miR10b using size exclusion chromatography, (top) UV trace at 254 nm, (bottom) radiodetector c. TEM of Cu-MN-anti-miR10b and natCu-MN-anti-miR10b d. Nanoparticle size by TEM and DLS. e. In vitro cell uptake by breast

adenocarcinoma cells. f. qRT-PCR demonstrating target engagement (inhibition of miR-10b). natCu was utilized for the preparation of natCu-MN-anti-miR10b. (t-test, n = 3, **P < 0.01).

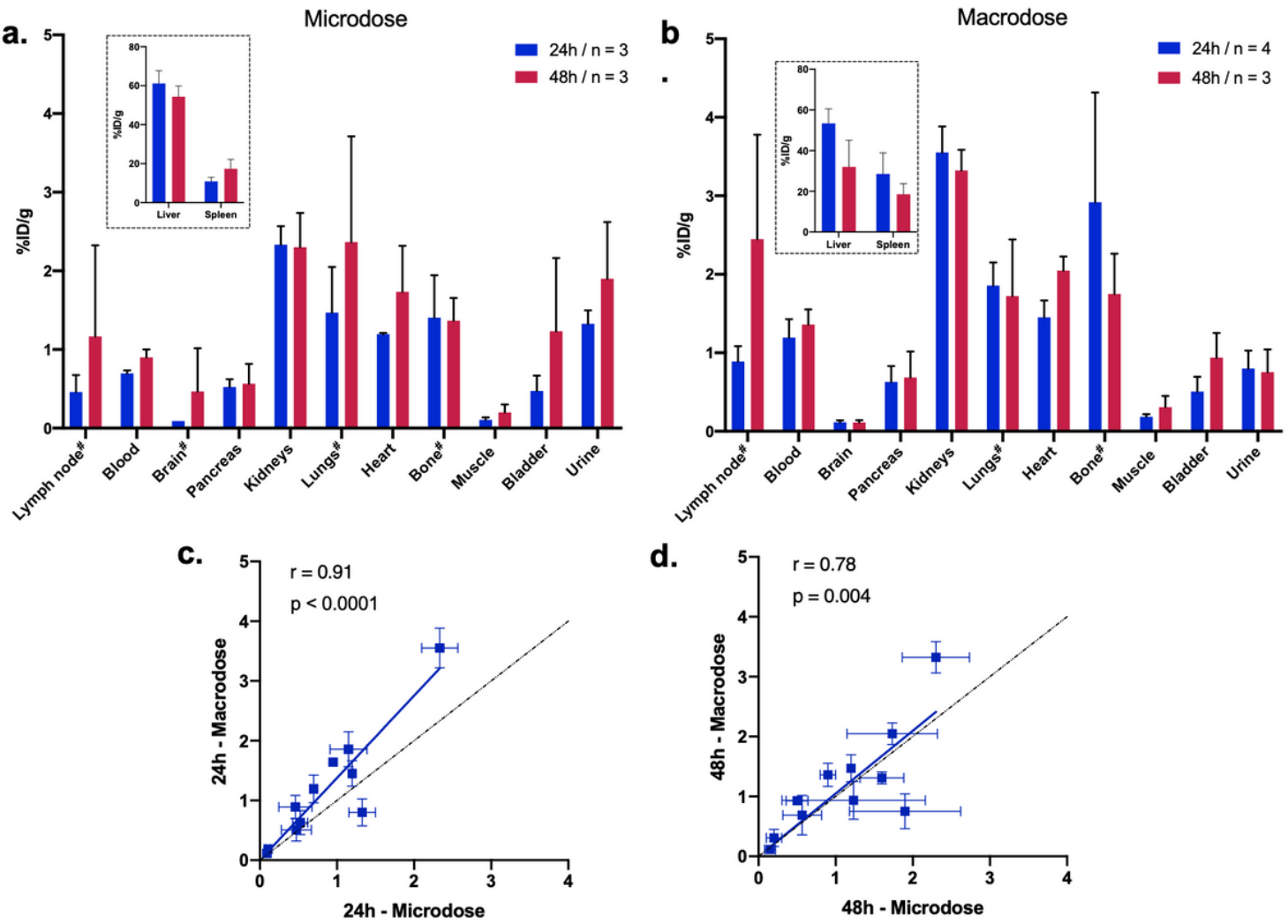


Figure 2

Ex-vivo biodistribution measured at 24 and 48 hours after administration of a. a microdose of 64Cu-MN-anti-miR10b (%ID/g), b. a therapeutic carrier-added macrodose of 64Cu-MN-anti-miR10b (%ID/g). # Denotes organs with metastasis as detected by BLI. Error bars represent standard error of the mean. Correlation between the %ID/g in non-metastatic organs obtained after administration of a microdose and the %ID/g obtained after administration of a macrodose at c. 24h and d. 48h post injection. (c and d: Pearson product-moment correlation, the dashed line corresponds to the line of identity).

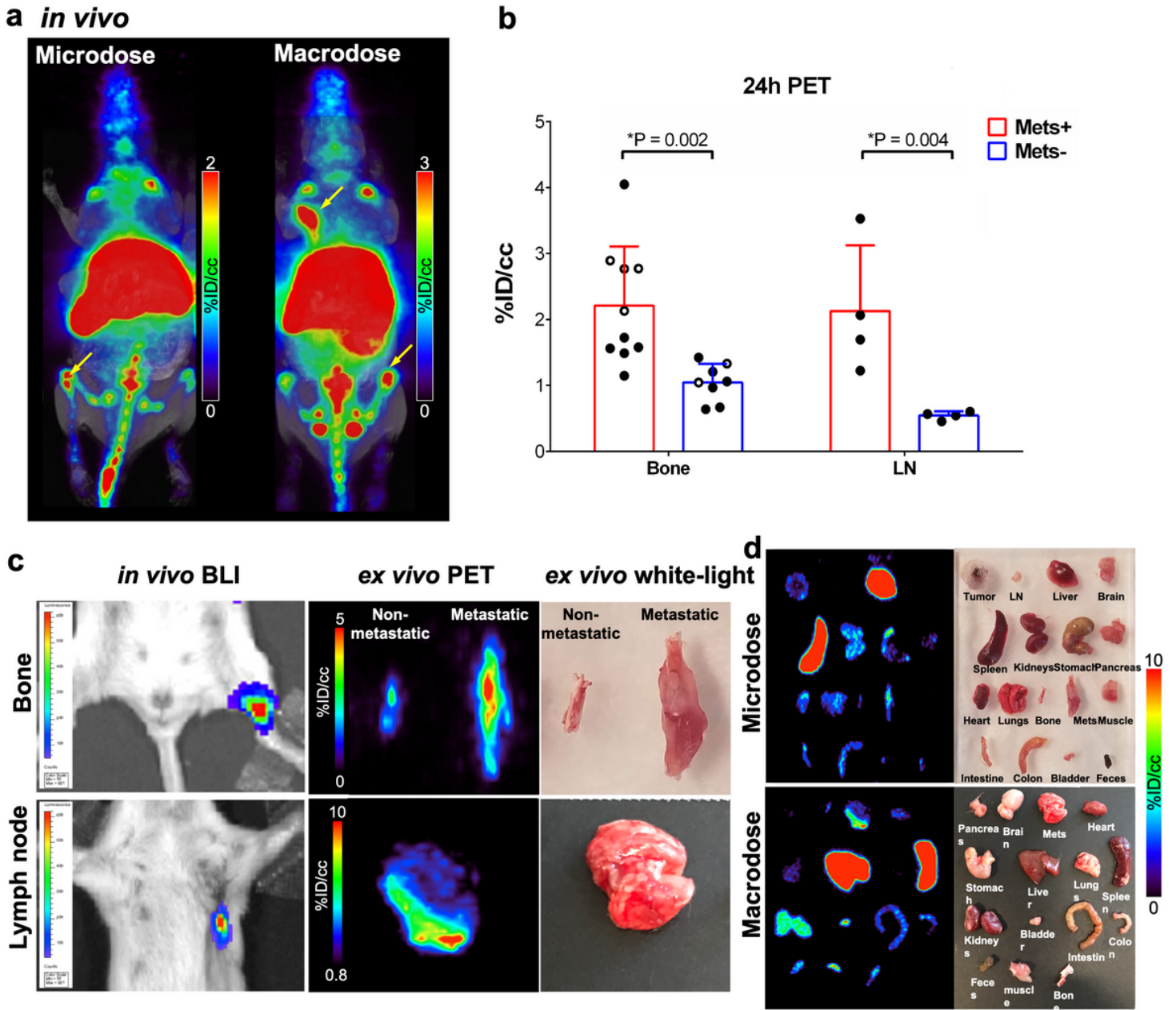


Figure 3

PET-MRI of ^{64}Cu -MN-anti-miR10b uptake by metastatic lesions. a. In vivo PET-MRI maximum intensity projection (MIP) images of mice bearing metastatic breast adenocarcinoma 24 hrs after injection of a microdose or a macrodose of ^{64}Cu -MN-anti-miR10b. The yellow arrows point to bone or lymph node (LN) metastasis. b. Quantitation of ^{64}Cu -MN-anti-miR10b accumulation in metastatic (Mets+) and non-metastatic (Mets-) organs obtained from in vivo PET images at 24 hrs post injection (%ID/cc). The high signal intensity in the metastatic organs compared to the non-metastatic organs confirms uptake of the therapeutic by the metastases. Open circles represent mice injected with a microdose and closed circles represent mice injected with a macrodose. c. Ex vivo PET-MRI of bone and lymph node metastases. From left: in vivo BLI, ex vivo PET, and ex vivo white-light photograph of metastatic lesions. d. Ex vivo

biodistribution of 64Cu-MN-anti-miR10b as visualized by PET 48 hrs after microdose injection and 24 hrs after macrodose injection.

Supplementary Files

This is a list of supplementary files associated with this preprint. Click to download.

- [CoverLettersigned.docx](#)
- [FigS1.png](#)
- [FigS2.png](#)
- [FigS3.png](#)
- [SuplInfo.docx](#)